AFRL-AFOSR-VA-TR-2023-0429

Refinement and Validation of Radiation Pressure Models for High Area-To-Mass Ratio Space Objects for Improved Characterization, Tracking, and Orbit Prediction

Jah, Moriba
UNIVERSITY OF TEXAS AT AUSTIN
110 INNER CAMPUS DR
AUSTIN, TX, 78712
USA

08/21/2023
Final Technical Report

Air Force Research Laboratory
Air Force Office of Scientific Research
Arlington, Virginia 22203
Air Force Materiel Command

REPORT DOCUMENTATION PAGE

PLEASE DO NOT RETURN YOUR FORM TO THE ABOVE ORGANIZATION.

1. REPORT DATE	2. REPORT TYPE	3. DATES COVERED	
20230821	Final	START DATE 20180501	END DATE 20210831

4. TITLE AND SUBTITLE
Refinement and Validation of Radiation Pressure Models for High Area-To-Mass Ratio Space Objects for Improved Characterization, Tracking, and Orbit Prediction

5a. CONTRACT NUMBER	5b. GRANT NUMBER	5c. PROGRAM ELEMENT NUMBER
	FA9550-18-1-0351	61102F
5d. PROJECT NUMBER	**5e. TASK NUMBER**	**5f. WORK UNIT NUMBER**

6. AUTHOR(S)
Moriba Jah

7. PERFORMING ORGANIZATION NAME(S) AND ADDRESS(ES)
UNIVERSITY OF TEXAS AT AUSTIN
110 INNER CAMPUS DR
AUSTIN, TX 78712
USA

8. PERFORMING ORGANIZATION REPORT NUMBER

9. SPONSORING/MONITORING AGENCY NAME(S) AND ADDRESS(ES)	10. SPONSOR/MONITOR'S ACRONYM(S)	11. SPONSOR/MONITOR'S REPORT NUMBER(S)
Air Force Office of Scientific Research 875 N. Randolph St. Room 3112 Arlington, VA 22203	AFRL/AFOSR RTB1	AFRL-AFOSR-VA-TR-2023-0429

12. DISTRIBUTION/AVAILABILITY STATEMENT
A Distribution Unlimited: PB Public Release

13. SUPPLEMENTARY NOTES

14. ABSTRACT
The proposed research aims to develop methods to improve detection, tracking, identification, and characterization (detect/track/ID/characterize) of Resident Space Objects (RSOs) in the GEO regime. This research will focus on a class of RSOs known as High Area-To-Mass Ratio (HAMR) objects. Current state of the art in detecting, tracking, identifying, and characterizing HAMR objects is limited due to the dynamic mismodelling of non-gravitational forces acting on these objects. The proposed research shall aim to enhance the physical models that govern the behavior of HAMR objects, specifically the acceleration due to solar and Earth albedo, solar and Earth radiation, and possibly electrostatic charging effects (Lorentz force). Refined models will then be used to estimate features such as mass, shape, and albedo-area of HAMR objects, in an aim to characterize them with higher confidence levels. To validate the refined physical models and characteristics of HAMR objects, and show improvements in tracking and prediction accuracies, novel filtering techniques shall be employed to estimate the long-term dynamics and trajectories of these objects. In essence, every trajectory can be interpreted as a signal encoded with information of all perturbing effects. The goal of model validation will be to extract the relevant perturbations from the trajectory signal and do so in a way that can be used to improve trajectory predictions. To augment the validation, we will assess how well we can predict the flux reflected from the object as compared to measured fluxes.

15. SUBJECT TERMS

16. SECURITY CLASSIFICATION OF:			17. LIMITATION OF ABSTRACT	18. NUMBER OF PAGES
a. REPORT U	b. ABSTRACT U	c. THIS PAGE U	UU	13

19a. NAME OF RESPONSIBLE PERSON	19b. PHONE NUMBER *(Include area code)*
MICHAEL YAKES	00000000

Standard Form 298 (Rev.5/2020)
Prescribed by ANSI Std. Z39.18

Technical Report

Accomplishments

- Original Research Objectives:
  - Rigorously quantify the various contributors to the probability of detection and assess the limits on detectability imposed by a lack of knowledge regarding the physical characteristics of a given Anthropogenic Space Object (ASO) and its environment.
  - Achieve the ability to remotely infer the mass of ASO from the mutual information content of the same contained within the combination of both astrometric and photometric data, and use this as a "feature" to aid in unique ASO identification.
  - Assess the possibility of determining an upper bound to the finite information content within any given set of data and understand when information dilution occurs and why, and how to mitigate this effect.
- Refined Research Objectives (because we determined that more fundamental research was required)
  - Quantify the theoretical bound on information about ASOs that can be extracted from measured photons
  - Experimentally characterize the information channel and Quanta Photogrammetry (QPM) receiver's properties to be used in the information theoretical study
  - Assess the degree to which ASO characterization and identification can be performed via QPMs and a biometrically-inspired recognition system
  - Assess the ability to translate the ASO features registered in the QPM to a dynamic model that can be shown to yield accurate trajectory and behavior predictions
  - Assess the degree to which no *a priori* or so-called uninformative priors can be used and how this affects the statistical inference process

- Details of accomplishments:
  - We successfully developed the QPM framework from real photon measurements
  - We successfully determined the spin states of an ASO from QPM, for the first time ever
  - We have demonstrated consistency between theoretical and experimental results regarding QPM
- Results of this can be found here: **Kucharski, D**., Kirchner, G., **Jah, M.**, Bennett, J., Koidl, F., Steindorfer, M., Wang, P. (2021). Full attitude state reconstruction of tumbling space debris TOPEX/Poseidon via light-curve inversion with Quanta Photogrammetry,

Acta Astronautica, https://doi.org/10.1016/j.actaastro.2021.06.032

Impacts

This QPM method is being considered for commercialization within our Biometrically-Inspired Space Object Recognition (BISOR) method, delivering on the first remotely sensed method to achieve unique ASO identification.

Changes

Nothing to Report

Technical Updates

Nothing to Report

Available online at www.sciencedirect.com

ScienceDirect

Advances in Space Research 63 (2019) 404–416

ADVANCES IN SPACE RESEARCH (a COSPAR publication)

www.elsevier.com/locate/asr

Reconciling space object observed and solar pressure albedo-areas via astrometric and photometric data fusion

Vishnuu Mallik *, Moriba K. Jah

Graduate Student, Aerospace Engineering and Engineering Mechanics Department, Cockrell School of Engineering, The University of Texas at Austin, Austin, TX 78712

Associate Professor, Aerospace Engineering and Engineering Mechanics Department, Cockrell School of Engineering, and Core Faculty, Institute for Computational Engineering and Sciences, The University of Texas at Austin, Austin, TX 78712

Received 7 October 2017; received in revised form 31 July 2018; accepted 3 August 2018
Available online 12 August 2018

Abstract

There are many Resident Space Objects (RSOs) in the Geostationary Earth Orbit (GEO) regime, both operational and debris. The primary non-gravitational force acting on these RSOs is Solar Radiation Pressure (SRP), which is sensitive to the RSO's area-to-mass ratio. Sparse observation data and mismodeling of non-gravitational forces has constrained the state of practice in tracking and characterizing RSOs. Accurate identification, characterization, tracking, and motion prediction of RSOs is a high priority research issue as it shall aid in assessing collision probabilities in the GEO regime, and orbital safety writ large. Previous work in characterizing RSOs has taken a preliminary step in exploiting fused astrometric and photometric data to estimate the RSO mass, shape, attitude, and size. This works, in theory, since angles data are sensitive to SRP albedo-area-to-mass ratio, and photometric data are sensitive to shape, attitude, and observed albedo-area. By fusing these two data types, mass and albedo-area both become observable parameters and can be estimated as independent quantities. However, previous work in mass and albedo-area estimation has not quantified and assessed the fundamental physical link between SRP albedo-area and observed albedo-area. The observed albedo-area is always a function of the SRP albedo-area along the line of sight of the observer. This is the physical relationship that this current research exploits. It is shown through simulation that due to this physical link, and through the fusion of astrometric and photometric data, it is possible to observe the mass of a space object when the area is not known. Results for data from 100 trajectories generated from randomly sampled initial conditions are shown. It is seen that even when the area of the object is not known, the uncertainty in mass can be lowered from an initial value of 800 kg to the range 500–700 kg for 72% of the samples, 200–500 kg for 13% of the samples, and 0–200 kg for 15% of the samples. It is further shown that although the uncertainties are large, the actual errors in mass are much lower, with the error RMS being less than 100 kg for 30% of the samples, between 100 and 200 kg for another 30%, and between 200 and 300 kg for 24% of the samples.

Keywords: Solar radiation pressure; Non-resolved object characterization; Astrodynamics; Data fusion; Space debris; Space situational awareness

1. Background and motivation

Advances in space technology, coupled with an increased dependence on space-based assets for both military and commercial purposes has led to a dramatic increase in the space object (SO) population since the first man-made object, Sputnik, was launched. A majority of these space objects is space debris, which consists of inactive satellites and debris that have been created due to collisions, explosions, and components breaking off over time due to space object aging (RSO gerontology). The Space Surveillance Network currently maintains a catalog of over

* Corresponding author.
E-mail addresses: vishnuu.mallik@utexas.edu (V. Mallik), moriba@utexas.edu (M.K. Jah).

https://doi.org/10.1016/j.asr.2018.08.005
0273-1177/

23,000 objects that are larger than 10 cm in diameter all the way up to the International Space Station. Only about 1500 of these objects are active space assets. Due to the need for meeting safety requirements for manned spaceflight, the debris population in low Earth orbit (LEO) has gained much of the research focus thus far. This, along with the fact that the LEO debris population can be studied from both radar and optical observations, has allowed researchers to achieve some meaningful understanding of the space environment and force models that govern the behavior of LEO space debris (Schildknecht et al., 2004). However, there is still work to be done for characterizing the debris population and environment in higher Earth orbits. Due to the larger search space, limited observations, and limitations in sensor technology, it is a non-trivial task to detect, track, and characterize debris in higher Earth orbits, let alone, be able to accurately predict their long-term orbital motion and behavior. Fig. 1 shows data obtained from the Defense Advanced Research Projects Agency's (DARPA) Space Surveillance Telescope. The data demonstrates that although a large number of objects have been detected in high Earth orbits, there remains a significant population of objects that have not been correlated to known objects, hence demonstrating that there are gaps in the current body of knowledge and the techniques used to study space objects that need to be filled. In other words, detecting an object and tracking an object are not equivalent. Tracking an object requires that the object be (a) detected and (b) uniquely identified, making tracking at best as difficult as detection and at worse much more challenging.

In order to be able to characterize dynamic and physical attributes of an RSO one must obtain measurements that provide information on those attributes. In order to demonstrate accurate characterization, one must be able to accurately predict future behavior based on accurate estimates of those attributes derived from observations. To that end, one of the major capabilities that needs to be filled is the accurate modeling of non-gravitational forces acting on objects in the near-Geostationary Earth Orbit (GEO). Such non-gravitational forces include Solar Radiation Pressure (SRP), Thermal Emissions, Outgassing, and Electromagnetic interactions. SRP is the primary non-gravitational force acting on objects in GEO, and improved modeling of SRP shall enhance the ability to predict the behavior and the spatio-temporal evolution of RSOs in the near-GEO regime. McMahon and Scheeres (2015) have shown how improved modeling of SRP results in improvements in tracking space objects. Improved characterization of RSOs entails acquiring improved estimates of an RSO's physical features, such as mass, area, shape and size. Previous work (Linares et al., 2014) in this area has shown that under idealized assumptions it is possible to infer an object's mass and albedo-area through the mutual information content obtained by fusing astrometric and photometric data. The research results provided here builds upon work done by Linares et al. (2014), extending it to using physically consistent BRDF models for both the acceleration due to SRP formulation and the light curve formulation. The need for this was recognized by Wetterer et al. (2013). The current research also exploits the physical link between the albedo-area estimated through the dynamic mismodeling of SRP and the observed albedo-area obtained directly via the measured light curve data.

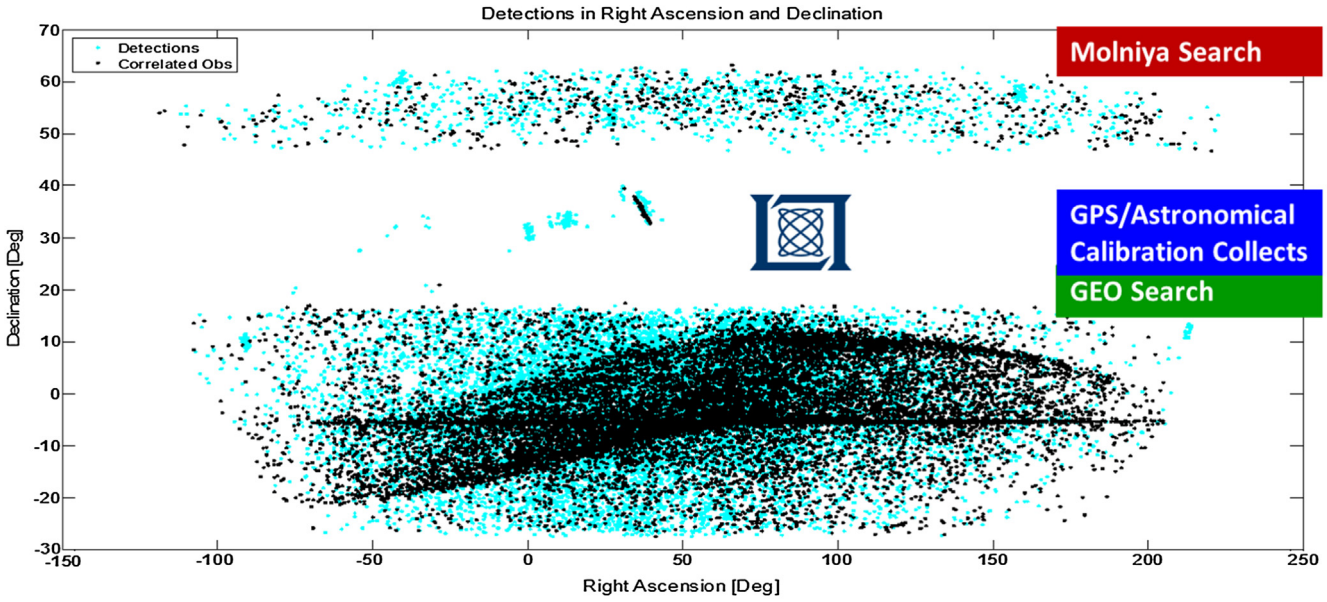

Fig. 1. Space Surveillance Telescope Synoptic Search Data. Tracked objects are shown in black, and detected objects (i.e. objects of unknown identity) are shown in Cyan (Jah, 2017). (For interpretation of the references to color in this figure legend, the reader is referred to the web version of this article.)

2. Data fusion

Space Situational Awareness (SSA) involves the acquisition of information regarding the space environment, particularly man-made space objects, and the ability to understand and predict their behavior in order to ensure safety and security of active space assets (Joint Chiefs of Staff, 2013). Data fusion is a methodology that enables SSA, as it extracts knowledge gained from the mutual information of multiple sources to achieve refined estimates of position and identity of a space object (Jah and Madler, 2007). For the characterization and feature estimation problem, it is only through the fusion of astrometric and photometric data that one can estimate features such as mass (Linares et al., 2014). This is due to the underlying physics behind these two data types: Astrometric or angles data are sensitive to SRP albedo-area-to-mass ratio, and hence this quantity is observable from this data type. Photometric or light curve data are sensitive to the object's shape, attitude, and observed albedo-area properties. Using only a single one of these data types in the estimation process does not make mass an observable quantity, since otherwise mass cannot be separated from the albedo-area. However, by fusing the two data types, mass can be estimated separately because the observed albedo-area is always a function of the SRP albedo-area onto the observer's line of sight vector to the SO (Linares et al., 2014) as shall be subsequently shown.

3. Albedo-area from SRP and light curves: the physical connection

In general, SRP is the main perturbing non-gravitational force experienced by objects at an altitude over 1000 km. The force due to SRP has a complex formulation that depends on the attitude of the space object and its distance from the Sun, as well as the geometry and optical properties of each surface of the object. It is caused by the net effect of absorption, reflection, and transmission of photons striking and leaving the space object. Fig. 2 depicts

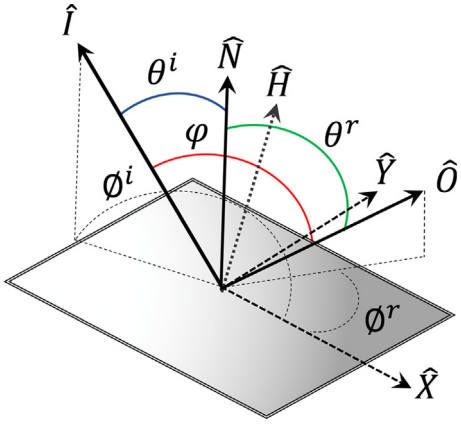

Fig. 2. Geometry of reflection from a single facet.

the geometry of reflection from a single facet (Wetterer et al., 2013), where and $\hat{Y}$ are unit vectors in the plane of the facet, $\hat{N}$ is the normal unit vector to the surface of the facet, and together, $\hat{X}$, $\hat{Y}$, and $\hat{N}$, along with their common origin, describe the body frame reference axes of the facet. $\hat{I}$ is the unit vector from the center of the facet to the illumination source (oriented at angle θ^i from $\hat{N}$ and $\varnothing^i$ from), $\hat{O}$ is the unit vector from the center of the facet to the observer (oriented at angle θ^r from $\hat{N}$ and $\varnothing^r$ from), and $\hat{H}$ is the half angle (bisector) vector between the illumination source and observer unit vectors. The angle between the illumination source, the object, and the observer is the phase angle, φ.

In its most general form, the acceleration due to SRP can be written as cf. (Wetterer et al., 2013)

$$a_{SRP} = -\sum_{i=1}^{N_{facets}} \int_0^{\infty} \frac{F_k(\lambda) A_i f_i (\hat{I}\cdot\hat{N}_i)_+}{mc} \times \left(\hat{I} + \left(\int_0^{2\pi}\int_0^{\pi/2} f^{BRDF}\cos\theta^r \hat{O} d\theta^r d\varphi^r\right)_i\right) d\lambda. \quad (1)$$

In the above equation, the subscript i on the variables denotes the value of that variable for a particular facet, F_k is the solar flux, A is the area of the facet, f is the fraction of the facet that is illuminated due to self-shadowing, m is the mass of the SO, c is the speed of light and λ is wavelength of light. This formulation models the surface of the SO as a combination of N number of facets, denoted as N_{facets} and hence the total acceleration due to SRP is expressed as a sum of the acceleration over all the facets, integrated over all the wavelengths of light, and over all observer directions. The positive subscript on $(\hat{I}\cdot\hat{N}_i)$ denotes that the acceleration due to SRP is zero if $(\hat{I}\cdot\hat{N}_i)$ is less than or equal to 0, which indicates that the facet is not illuminated. In Eq. (1), f^{BRDF} is the Bidirectional Reflectance Distribution Function (BRDF), where

$$f^{BRDF} = (dR_d + sR_s). \quad (2)$$

In Eq. (2), for a particular facet, R_d is the diffuse bidirectional reflectance, R_s is the specular bidirectional reflectance, and d and s are the fraction of the reflected photons that are diffusely and specularly reflected, respectively. The total BRDF is calculated as the sum of these two quantities, which are both dependent on the illumination source and direction, the observer direction, and the surface properties of the object. The BRDF defines how incoming photons interact with and reflect from any given surface of an object, and is an integral term of the SRP formulation. The dependence on the SO's attitude is indirectly incorporated into the BRDF formulation through the illumination and observer direction from the normal unit vector of the facet under consideration. The RSO used in this study is modeled as an object whose surface reflectance properties can be represented using a BRDF that has a

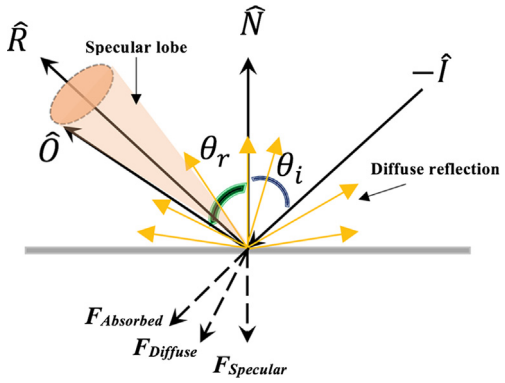

Fig. 3. Reflection geometry and forces due to incident radiation off a single facet.

Lambertian diffuse component and a perfectly specular or 'mirror-like' component. Such a BRDF is given by (Wetterer et al., 2013)

$$f^{BRDF} = d\left(\frac{\rho}{\pi}\right) + s\left(\frac{F_0\Delta(\hat{O}-\hat{R})}{\cos\theta^i}\right) \tag{3}$$

where ρ is the diffuse reflectance and F_0 is the Fresnel reflectance at normal incidence. In Eq. (3), $\Delta(x)$ denotes the delta function, which is 0 everywhere except $\Delta(0)$. Fig. 3. depicts the reflection geometry from a surface of a single facet due to incoming radiation for the case of Lambertian diffuse and near-perfect specular reflection. Here, $\hat{R}$ is the direction of perfect "mirror-like" specular reflection, and the conical lobe around it depicts the lobe of near-perfect specular reflection due to material properties and irregularities. In the development of SRP acceleration used for the research presented here, a similar approach as taken by Lyon (2002) is followed, where transmissivity is assumed to be zero[1], and the coefficient of absorptivity, specular reflectivity, and diffuse reflectivity are related by the constraint

$$C_{Abs} + C_{Diff} + C_{Spec} = 1 \tag{4}$$

where C_{Abs} is the coefficient of absorption, C_{Spec} is the coefficient of specular reflection, and C_{Diff} is the coefficient of diffuse reflection. Part of the radiation that is incident on the surface is directly absorbed by the surface, and the momentum imparted by the photons that are absorbed into the surface causes a force in the direction of incident radiation. The force due to this fraction of incident radiation on a single facet of area A is given by

$$F_{Absorbed} = -\frac{F_{sun}A\cos\theta^i}{c}C_{Abs}\hat{I}. \tag{5}$$

The incident radiation that is not absorbed by the surface is reflected, partly in a specular manner, and partly in a diffuse manner. The intensity and geometry of the specular and diffuse reflection depend on the material and surface properties of the reflecting surface. The momentum exchange caused due to photons reflected specularly and diffusely cause a net diffuse and specular force on the surface, the direction of which depends on the geometry of reflection and ratio of specular to diffuse reflectivity. For the case shown in Fig. 3, the near-perfect specular reflection causes a net force in the direction opposite to the surface normal, and the Lambertian diffuse reflection causes a force that is partly in the direction of incident radiation and partly in the direction opposite to the surface normal. The force due to specular reflection is given by

$$F_{Specular} = -\frac{F_{sun}A\cos\theta^i}{c}2\cos\theta^i C_{Spec}\hat{N} \tag{6}$$

and that due to diffuse reflection by

$$F_{Diffuse} = -\frac{F_{sun}A\cos\theta^i}{c}C_{Diff}\left(\hat{I}+\frac{2}{3}\hat{N}\right). \tag{7}$$

The total force on a surface due to incoming radiation is hence the net force due to absorption, specular reflection, and diffuse reflection, which can be written as

$$F_{SRP} = F_{Absorbed} + F_{Specular} + F_{Diffuse} \tag{8}$$

which when expanded using Eqs. (5)–(7) gives

$$F_{SRP} = -\frac{F_{sun}A\cos\theta^i}{c} \times \left[C_{Abs}\hat{I} + C_{Diff}\hat{I} + 2C_{Spec}\cos\theta^i\hat{N} + \frac{2}{3}C_{Diff}\hat{N}\right]. \tag{9}$$

Due to the constraint in Eq. (4), the absorptivity coefficient can be written in terms of specular and diffuse reflectivity as

$$C_{Abs} = 1 - C_{Diff} - C_{Spec}. \tag{10}$$

Applying Eq. (10) to Eq. (9), we have the total force due to SRP on a single facet as

$$F_{SRP} = -\frac{F_{sun}A\cos\theta^i}{c} \times \left[(1-C_{Spec})\hat{I} + \left(\frac{2}{3}C_{Diff} + 2C_{Spec}\cos\theta^i\right)\hat{N}\right]. \tag{11}$$

This results in an acceleration due to SRP (summed over all the facets of the RSO) of

$$a_{SRP} = -\sum_{i=1}^{N_{facets}}\frac{F_{sun}A_i\cos\theta_i^i}{mc} \times \left[(1-C_{Spec})_i\hat{I} + \left(\frac{2}{3}C_{Diff} + 2C_{Spec}\cos\theta^i\right)_i\hat{N}_i\right]. \tag{12}$$

This formulation of the acceleration due to SRP is similar to that obtained from analytically solving Eq. (1) with the BRDF shown in Eq. (3) (Wetterer et al., 2013) and is used for facet-based modeling of spacecraft (Ziebart, 2004). Note that this formulation does not take into account self-shadowing.

The BRDF is essential in modeling photometric data, or light curves. A light curve is the temporal history of an

[1] i.e. in future work to be handled via the modeling of a Bidirectional Transmission Distribution Function [BTDF].

object's wavelength-dependent observed brightness, or apparent magnitude (Wetterer and Jah, 2009). The observed brightness of an object is a function of the number and direction of the photons that are reflected off the surface, which itself is a function of the illumination source, the number and direction of the incoming photons, and the wavelength(s) being measured by the sensor used to observe it. Synthetic light curves can be used to model the observed brightness of an object given the object's shape, size, and attitude, by representing the physics that determines the object's reflectance properties, i.e. a BRDF. Essentially, a light curve model uses a BRDF to determine the number of photons that are reflected in the direction of the observer. This in combination with atmospheric extinction, for example, will determine the notional quantities of photons that can be measured. To generate synthetic light curves for a facet based model (Linares et al., 2014), first the fraction of reflected sunlight from each facet is calculated through

$$S_i^{reflected} = F_{Sun} f_i^{BRDF}(\hat{N}_i \cdot \hat{I}). \tag{13}$$

Then the fraction of reflected light that is reflected along the direction of the observer (what the observer sees) is calculated by

$$S_i^{observed} = \frac{S_i^{reflected} A_i(\hat{N}_i \cdot \hat{O})}{r^2} \tag{14}$$

where r is the distance between the RSO and the observer. Finally, the apparent brightness of the object is computed by

$$m_{object} = m_{sun} - 2.5\log_{10}\left(\sum_{i=1}^{N_{facets}} \frac{S_i^{observed}}{F_{Sun}}\right) \tag{15}$$

where m_{sun} is the apparent magnitude of the Sun for a given band pass (which in the case of visible light is -26.7). Eq. (15) can also be written as (Wetterer and Jah, 2009)

$$m_{object} = m_{sun} - 2.5\log_{10}\left(\sum_{i=1}^{N_{facets}} \frac{f_i^{BRDF} A_i(\hat{N}_i \cdot \hat{I})(\hat{N}_i \cdot \hat{O})}{r^2}\right). \tag{16}$$

It is important to note that to accurately model both the acceleration due to SRP and light curves for an object, the same BRDF must be used in both formulations because how a surface scatters energy is independent of a passive observer. If C_R is used to denote the albedo of a surface, where albedo is a variable that describes how a surface reflects incident light, then the acceleration due to SRP is a function of the albedo-area of the RSO projected along the direction of the Sun, termed SRP albedo-area and denoted by K_{SRP}. For a single facet, the area of the facet that contributes to the acceleration due to SRP is $A(\hat{I} \cdot \hat{N})$, and hence the SRP albedo-area is given by the relation

$$K_{SRP} = (C_R)A(\hat{I} \cdot \hat{N}). \tag{17}$$

Note that this quantity in itself is not observable through astrometric data, but rather SRP albedo-area-to-mass ratio. Now the observed albedo-area, denoted by K_{OBS}, is the albedo-area that a passive observer can see, and is dependent on the fraction of light that is reflected, and the albedo-area that is projected along the line of sight of the observer i.e.

$$K_{OBS} = (C_R)A(\hat{I} \cdot \hat{N})(\hat{N}.\hat{O}). \tag{18}$$

Eqs. (17) and (18) are hence related through

$$\frac{K_{OBS}}{\cos\theta^r} = K_{SRP} \tag{19}$$

This relationship is the main physical relationship that this work exploits, and is depicted in Fig. 4 to provide more clear insight.

As shown in Fig. 4, the phase angle is defined as the angle between the unit vector from the SO along the line of sight of the observer and the unit vector from the SO in the direction of the Sun. At lower phase angles, the SRP albedo-area and observed albedo-area should have better agreement, and in theory, at 0-degree phase angle, the two are exactly the same. In other words, at very low phase angles, the light curve data provides a direct measurement of the SRP albedo-area. On the other hand, at 90-degree phase angle, there is no signal, i.e. the physical relationship between the albedo-area that the Sun sees

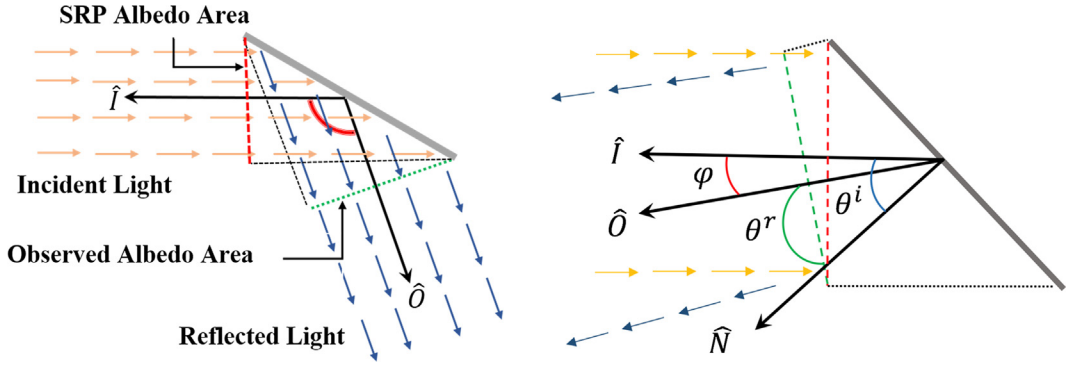

Fig. 4. Reflection from a single facet, showing SRP albedo-area and observed albedo-area.

and the albedo-area seen by an observer cannot be reconciled geometrically.

4. Methodology

Due to the fact that the observed albedo-area is always a function of the SRP albedo-area, and that the observed albedo-area is directly observable through light curves, we can get precise estimates of mass and albedo-area. To demonstrate this, we shall show results for estimating mass and albedo-area for an RSO with surface reflectance properties that can be modeled using the BRDF shown in Eq. (3).

The RSO used for this work is modeled as a 3-axis stabilized, Sun-pointed flat plate. For this work, the attitude is assumed to be known. Although this is a highly idealistic simplification, the purpose of this work is to show how accurately we can estimate mass and albedo-area by directly measuring an estimated quantity which is justified through the physical relationship that has been discussed in previous sections. Moreover, Wetterer and Jah (2009) have demonstrated that the attitude of an object can be estimated using light curve data. However, it is in the scope of future work to include an assessment of attitude errors in the estimation process. Another simplification that this work employs is that the RSO is modeld as a flat plate and it's entire surface can be modeled using the same BRDF. This may be true for a small population of objects, but most objects would have to be modeled as complex shapes with different surface reflectance properties. In that case, it would become necessary to corellate emperical light curves to analytical ones to assess what combination of analytical BRDFs provide the best fit for emperical light curve data, and possibly come up with hybrid BRDFs. This too is in the scope of future work.

4.1. SRP model and analytical light curve formulation

The SRP formulation shown in Eq. (12) is used in this work, except it is now written in terms of d, ρ, s, and F_0 (Wetterer et al., 2013) as

$$a_{SRP} = -\sum_{i=1}^{N_{facets}} \frac{F_{sun} A_i (\widehat{I}\cdot\widehat{N}_i)_+}{mc} \times \left((1 - s_i (F_0)_i)\widehat{I} + \left(\frac{2}{3}(d\rho)_i + 2(sF_0)_i (\widehat{I}\cdot\widehat{N}_i) \right) \widehat{N}_i \right). \tag{20}$$

Light curves were generated in the visible-light bandpass by computing the apparent brightness magnitude of the object in the direction of the observer through Eq. (16). The BRDF in Eq. (3) is used as the BRDF for light curve modeling in the estimation filter to ensure physical consistency between the acceleration due to SRP and light curve formulation. However, the BRDF in Eq. (3) is slightly modified for our purpose, since in its original form, the specular component only contributes when the phase angle is 0 degrees, or when the normal and bisector vectors are aligned, which results in glints. From a practical standpoint, the specular component contributes to the total BRDF when the $\widehat{O}$ and $\widehat{R}$ direction are less than or equal to about 10 degrees. Hence, in its modified form, the BRDF we use for light curve modeling in the filter for this work is given by

$$f_i^{BRDF} = d_i \left(\frac{\rho}{\pi}\right)_i + s_i \left(\frac{F_0 H(\widehat{O},\widehat{R})}{\cos\theta^i} \right)_i \tag{21}$$

where

$$H(\widehat{O},\widehat{R}) = \begin{cases} 1 & a\cos(\widehat{O}\cdot\widehat{R}) \leqslant 10^\circ \\ 0 & a\cos(\widehat{O}\cdot\widehat{R}) > 10^\circ \end{cases}. \tag{22}$$

This modification essentially creates a specular lobe when the angle between the direction of the observer and the direction of mirror like reflection is less than 10 degrees, which given the subject matter expertise of others in the community, is not unreasonable (Dr. Tamara Payne and Doyle Hall, personal communications). It is important to note that this 10 degree specular cone is the result of reflections from certain surface types such as solar panels, and depending on the surface type, this opening angle may differ.

4.2. Filtering technique

An Unscented Schmidt-Kalman Filter algorithm developed following the approach taken by Stauch and Jah (2015) was used in the estimation process. This is a version of the unscaled Unscented Kalman Filter (UKF) that incorporates the uncertainties due to certain parameters by treating them as consider parameters. Given the geometry of the problem and measurements, certain parameters may show poor observability, so treating these parameters as consider terms is able to take their uncertainties (provided they are "known or bounded") into account without estimating them (Stauch and Jah, 2015). The unscaled version of the UKF only differs from the scaled or more common version of the UKF by the fact that the mean value of the estimated parameters is eliminated from the sigma points, which in turn eliminates the tuning parameters. The lack of tuning parameters eliminates the complexity of correctly tuning the regular scaled UKF, and has shown better performance in processing real data (Stauch and Jah, 2015).

The estimated state parameters are

$$\widehat{X} = \begin{bmatrix} R & V & m & K_{diff} & \vdots & K_{spec} & A \end{bmatrix} \tag{23}$$

where R and V are the position and velocity states, m is the mass, K_{diff} and K_{spec} are respectively the diffuse and specular albedo-areas, and A is the area of the RSO. To ensure that the sigma-points are always physically realistic, the constraints given by Eq. (24) are imposed on the UKF in

accordance with the technique described by Kandepu et al. (2008).

$$\begin{aligned} &5\text{ kg} \leqslant \text{m} \\ &0 \leqslant (C_{Diff})_i \leqslant 1 \\ &0 \leqslant (C_{Spec})_i \leqslant 1 \\ &1\text{ m}^2 \leqslant (A)_i \end{aligned} \tag{24}$$

Lower bounds of 5 kg and 1 m^2 were arbitrarily picked since it is not physically possible for mass or area to be 0, and some physically realistic lower bound for the constraint boundary had to be chosen. The albedo-area's can be broken down and written in terms of diffuse and specular reflectivity terms as

$$(K_{diff})_i = (d\rho A)_i \tag{25}$$

and

$$(K_{spec})_i = (sF_0 A)_i. \tag{26}$$

For this work, the specular contribution to the albedo-area is only being estimated when the condition stated in Eq. (22) is met and is otherwise treated as a "consider" term, since the specular term only contributes to the apparent magnitude when the condition for a glint is met or the phase angle is less than 10 degrees. By treating K_{spec} as a "consider" parameter for the times when there is no specular contribution to albedo-area, we are able to analyze how including this parameter's uncertainty may affect the results of the estimation process, but not actually allow estimates of the parameter itself to affect our results since the value for this parameter is not updated in the corrective step of the filtering process. Similarly, the area of the RSO is treated as a consider parameter throughout the estimation process, since this parameter shows poor observability when estimating albedo-area as well (Linares et al., 2014).

Using this notation in Eqs. (3) and (16), the model used to estimate light curve data in the filter can be written in the form

$$m_{object} = m_{sun} - 2.5\log_{10}\left(\sum_{i=1}^{N_{facets}} \frac{F_{rA_i}(\hat{N}_i \cdot \hat{I})(\hat{N}_i \cdot \hat{O})}{r^2}\right) \tag{27}$$

where

$$F_{rA_i} = \left(\frac{K_{diff}}{\pi} + \frac{K_{spec}}{\cos\theta^i}\right)_i \tag{28}$$

is the combination of the BRDF and facet area terms. Similarly, the model used to estimate the acceleration due to SRP in the filter, which is given by Eq. (20), can be written as

$$\begin{aligned} a_{SRP} = &-\sum_{i=1}^{N_{facets}} \frac{F_{sun}(\hat{I} \cdot \hat{N}_i)_+}{mc} \\ &\times \left((A - K_{spec})_i \hat{I} + \left(\frac{2}{3}K_{diff} + 2K_{spec}(\hat{I} \cdot \hat{N})\right)_i \hat{N}_i\right). \end{aligned} \tag{29}$$

This formulation allows the albedo-areas estimated through the acceleration due to SRP by the filter to be fed in as an input into the estimated light curve measurement model, thereby ensuring consistency in albedo-areas. However, as can be seen in Eq. (29), it is not possible to separate the acceleration due to the $A_i\hat{I}$ term and write it as a function of specular and diffuse reflectances. It is in the scope of future work to investigate this and derive a solution, but for this work, the a priori value of the area is used for the A_i term, and as discussed previously, the uncertainty on area is accounted for by treating area as a consider parameter.

Along with light curve data, angles data in the form of azimuth (az) and elevation (el) are also used, and hence the measurement vector for the filter is given by

$$\hat{y} = [\, m_{object} \quad az \quad el \,] \tag{30}$$

5. Simulations and results

Reference trajectories were generated from 100 randomly sampled physical parameters and initial position and velocity state vectors. The physical parameters of the RSO were sampled using a mean and standard deviation provided in Table 1. The initial position and velocity of the RSO were sampled using a mean and standard deviation provided in Table 2. The mean values for the RSO physical and surface parameters and position and velocity were used as a priori knowledge in the filter, and the a priori covariance was formed using the standard deviation associated with each of the values.

Reference data were generated from these trajectories every 60 s for a total of 15 days starting Dec 21, 2010 at 05:00:00 UT from Maui, Hawaii. Data were only collected for a period of 12 h a day. Table 3 provides details of the

Table 1
RSO physical and surface reflectance parameters.

Parameter	Mean value	Standard deviation
Mass	1000 kg	800 kg
Area	64 m^2	32 m^2
$d\rho$	0.48	0.24
sF_o	0.12	0.06
K_{diff}	30.72 m^2	7.68 m^2
K_{spec}	7.68 m^2	1.92 m^2

Table 2
RSO initial conditions.

Parameter	Mean value	Standard deviation
X position	42256.778 km	100 km
Y position	2953.979 km	100 km
Z position	51.593 km	100 km
X velocity	−0.213 km/s	0.01 km/s
Y velocity	3.058 km/s	0.01 km/s
Z velocity	0.107 km/s	0.01 km/s

Table 3
Reference data and filter measurement noise settings.

Parameter	Reference data measurement noise	Filter measurement noise
m_{object}	0.1	0.2
az	1 arc second	2 arc seconds
el	1 arc second	2 arc seconds

simulated reference measurements as well as the measurement model used in the filter.

Figs. 5–9 show results for all 100 randomly sampled reference trajectory data. These results show that the filter is able to recover position and velocity well for all samples. Although for some samples, the position and velocity 3σ uncertainties evolve significantly (on the order of 1 km for position and 0.1 m/s for velocity), all the errors are well bounded by the uncertainties, and these large uncertainties evolve during the 12 h measurement gaps and are reduced once more measurements are processed. The albedo-areas are estimated with final uncertainties less than 0.5 m^2 for all samples, and show good observability throughout the estimation process. This is a result of estimating a quantity that is directly observed from light curve data. While the uncertainties on mass for all samples are reduced from the a priori values, the final uncertainties for 72% of the samples are in the range 500–700 kg. However, all the errors are well bounded, and as is revealed further, the larger uncertainties in mass can be correlated to the uncertainty in the area of the RSO. Figs. 10 and 11 show histograms of final uncertainties for mass and mass error RMS values. These further indicate that although most

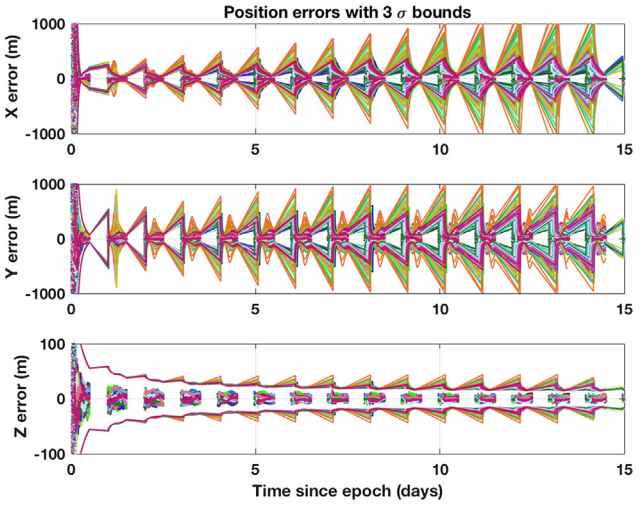

Fig. 5. Position errors with 3σ covariance envelopes for the case where area is treated as a consider parameter.

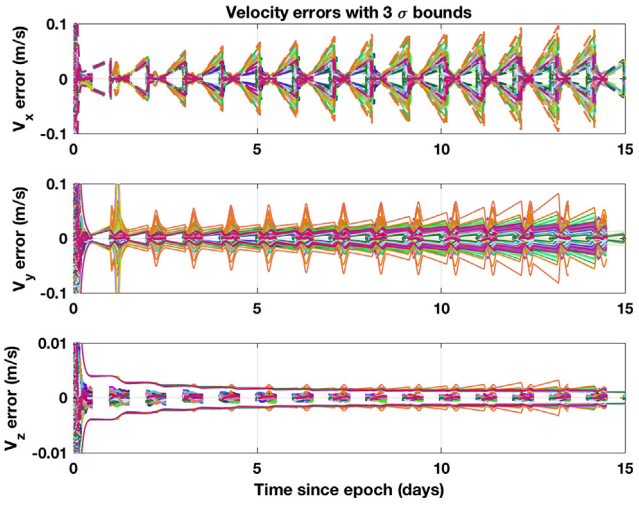

Fig. 6. Velocity errors with 3σ covariance envelopes for the case where area is treated as a consider parameter.

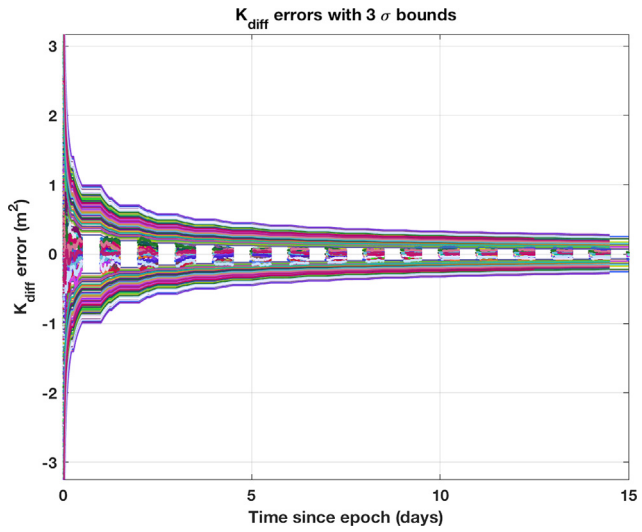

Fig. 7. Diffuse albedo-area errors with 3σ covariance bounds for the case where area is treated as a consider parameter.

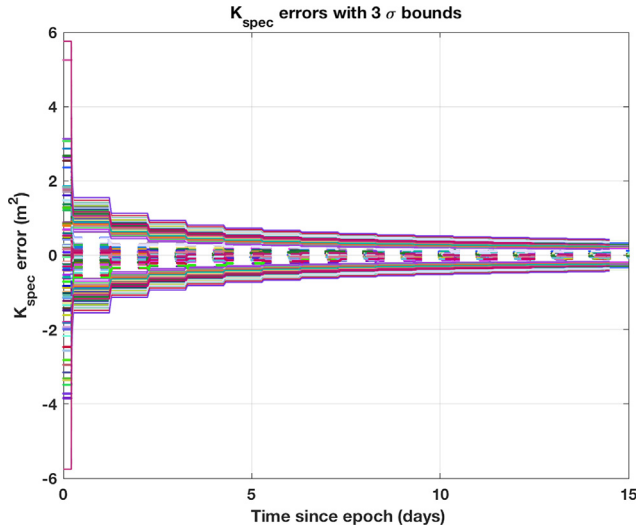

Fig. 8. Specular albedo-area errors with 3σ covariance bounds for the case where area is treated as a consider parameter.

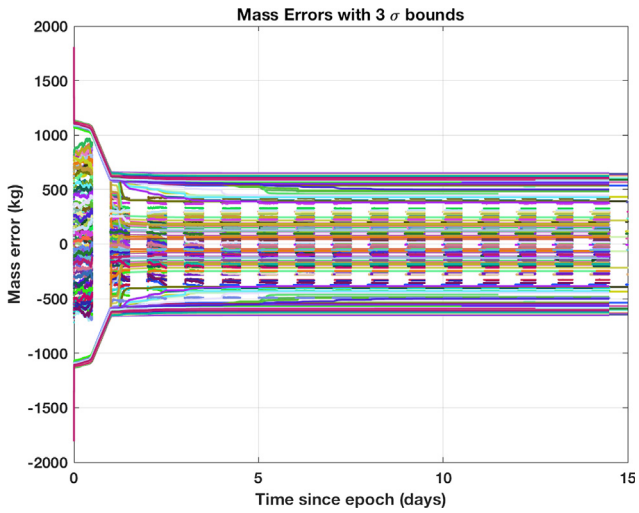

Fig. 9. Mass errors with 3σ covariance bounds for the case where area is treated as a consider parameter.

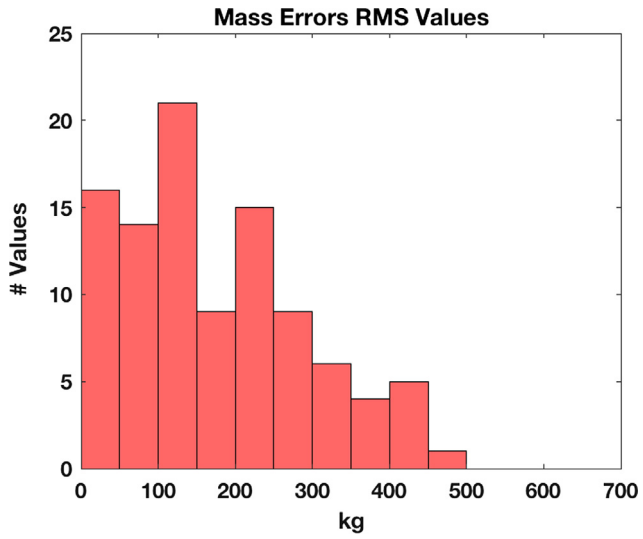

Fig. 11. Histogram of mass error RMS values.

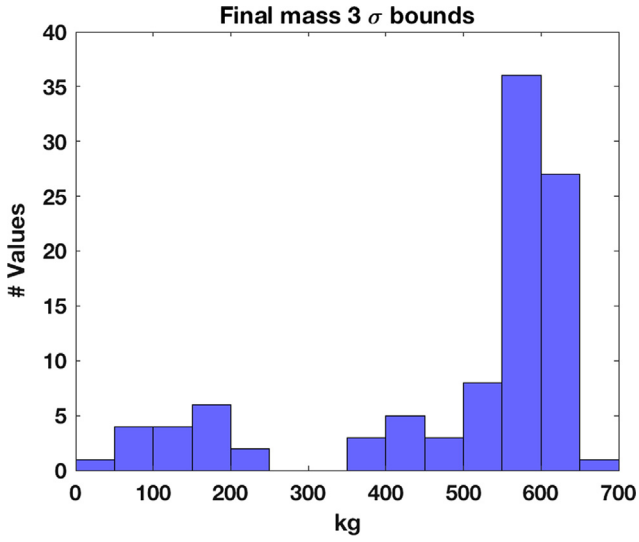

Fig. 10. Histogram of values for final 3σ uncertainty in mass.

samples show high final uncertainties, only 16% of the samples have an error RMS greater than 300 kg. 30% of the samples have an error RMS less than 100 kg, another 30% have an error RMS between 100 and 200 kg, and 24% have an error RMS between 200 and 300 kg. Similar statistics for the rest of the parameters, represented by histograms are provided in Appendix A.

Table 4 provides a summary of the final uncertainties for each of the estimated parameters. For each parameter uncertainty, the % values falling under specific bounds are listed.

To analyze the effect of not considering the area term, the UKF was run for the same set of data with the same settings, except now, area was not considered in the estimated state. Figs. 12–16 show results for this scenario for all 100 samples. The position and velocity diverge for some samples, as the errors are not bound by the 3σ covariance bounds. The diffuse and specular albedo-area errors are not estimated for any of the samples, as all of the errors are well outside the covariance bounds. For mass, although the errors behave similarly as for the case where area is considered (shown in Fig. 9), none of errors remain bounded by the 3σ covariance bounds through the course of the measurement span. Therefore, not considering area results in unrealistically low uncertainties for the states and fails to aid the RSO characterization effort for the case where the area of the object is not known.

Table 4
3σ parameter uncertainties for 100 samples.

Final position uncertainties			
	0–100 m	**100–300 m**	**300–600 m**
X Position 3σ	83%	17%	0%
Y Position 3σ	28%	70%	2%
Z Position 3σ	100%	0%	0%
Final Velocity Uncertainties			
	0–0.01 m/s	**0.01–0.03 m/s**	**0.03–0.07 m/s**
X Velocity 3σ	70%	30%	0%
Y Velocity 3σ	45%	52%	3%
Z Velocity 3σ	100%	0%	0%
Final Diffuse Albedo Area Uncertainties			
	0–0.1 m^2	**0.1–0.2 m^2**	**0.2–0.3 m^2**
K_{diff} 3σ	5%	57%	38%
Final Specular Albedo Area Uncertainties			
	0–0.25 m^2	**0.25–0.35 m^2**	**0.35–0.45 m^2**
K_{spec} 3σ	22%	67%	11%
Final Mass Uncertainties			
	0 0–200 kg	**200–500 kg**	**500–700 kg**
Mass 3σ	15%	13%	72%

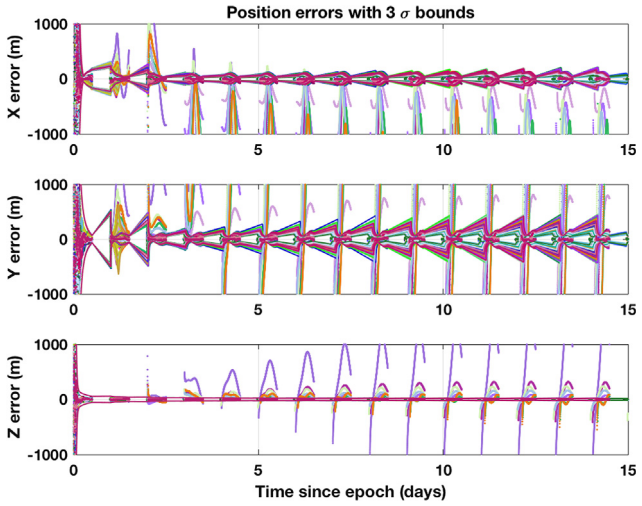

Fig. 12. Position errors with 3σ covariance envelopes for the case where area is not considered.

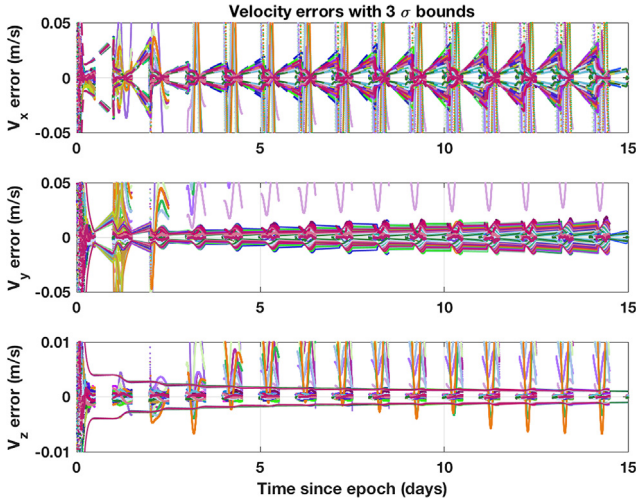

Fig. 13. Velocity errors with 3σ covariance envelopes for the case where area is not considered.

To validate if there is a correlation between the uncertainties on area and mass, reference trajectories and data were simulated using the same values provided in Tables 1 and 2, but with different standard deviations in area. Four such reference trajectories were generated with the standard deviations on area being 1%, 10%, 30% and 50% of the mean value. UKF mass estimate results for these cases are shown in Fig. 17. The time history of the cross correlation coefficient for mass and area for these cases is shown in Fig. 18. This shows that there is a positive correlation between the uncertainty on area and the uncertainty on mass. However, this is just a preliminary test to give some validity to this hypothesis. A more thorough investigation on how exactly the uncertainty on area effects mass, and what the upper bound for these uncertainties are, is in the scope of future work.

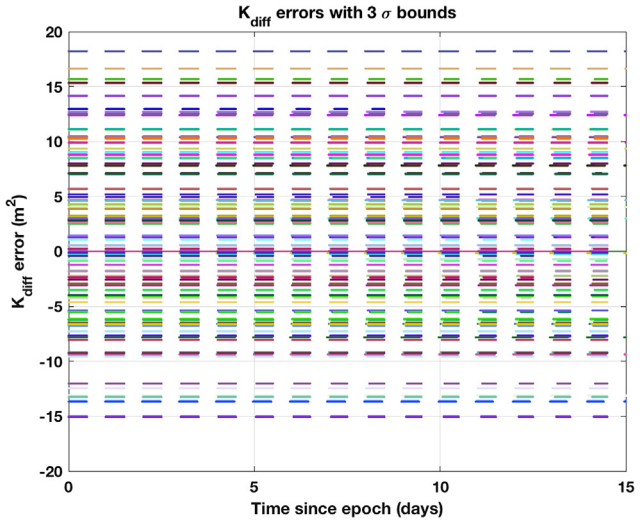

Fig. 14. Diffuse albedo-area errors with 3σ covariance envelopes for the case where area is not considered.

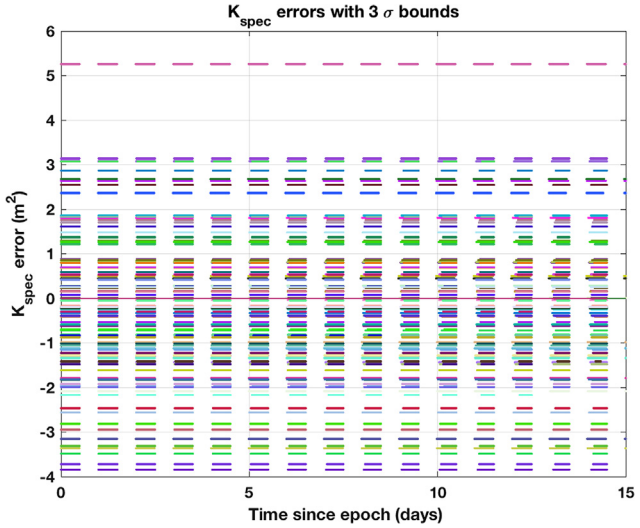

Fig. 15. Specular albedo-area errors with 3σ covariance envelopes for the case where area is not considered.

6. Future work

The work presented here was performed as a proof of concept and the simulations were idealized in the sense that the attitude was assumed to be known and was not estimated, the RSO model considered was a Sun-pointed flat plate, and a simple BRDF formulation was used for deriving the synthetic light curves and acceleration due to SRP. Future work would entail the following steps to create high-fidelity results with a more realistic scenario:

1. Estimating the RSO's attitude for the case of a non 3-axis stabilized attitude profile.

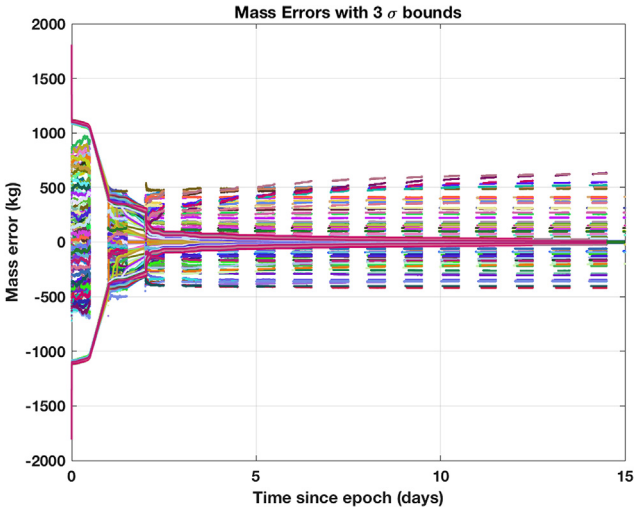

Fig. 16. Mass errors with 3σ covariance bounds for the case where area is not considered.

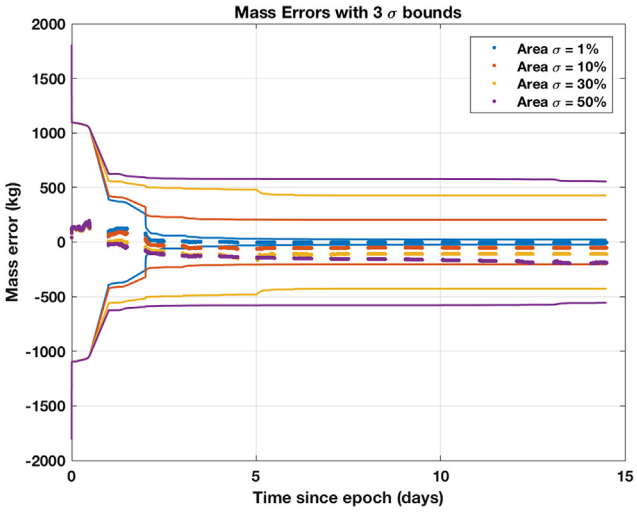

Fig. 17. Mass errors with covariance envelopes for different values of error in area.

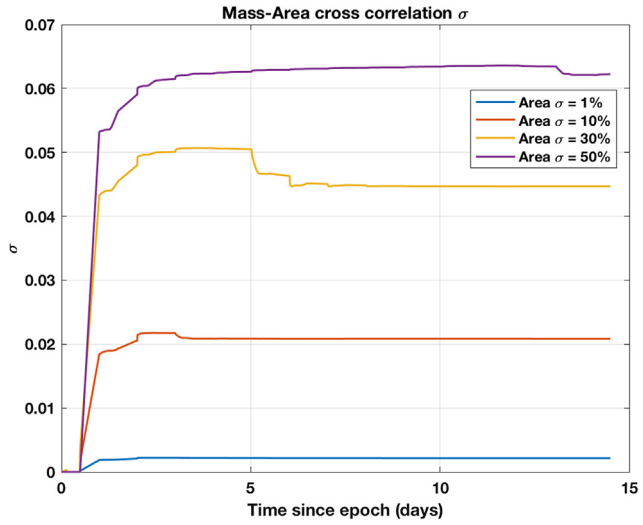

Fig. 18. Mass-Area cross correlation coefficient for different values of error in area.

2. Using a more sophisticated RSO model, such as a box wing with solar panels or other more representative RSO shape, and taking into consideration the self-shadowing factor in the SRP model.
3. Using other BRDFs such as Maxwell-Beard and Cook-Torrance that may be more representative of common GEO RSO material and surface properties, and using the approach developed by Wetterer et al. (2013) and Linares et al. (2013) to model solar radiation pressure for refined BRDF models.
4. Glint Analysis: Glints occur when the bisector vector and the normal are close to each other and/or at low phase angles. During glints, an object's brightness as viewed by the observer is dominated by its surface's specular reflectance properties, which causes sudden change in the apparent brightness of the object. Glints contain information regarding the specular reflectivity of an RSO's surface, and this information can be used in the estimation process to aid the RSO characterization effort.
5. Modeling the force caused due to the incident irradiance in the acceleration due to SRP formulation as a quantity that is dependent on other estimated parameters, hence allowing the single area term that cannot be written as a function of albedo to be estimated as well.

7. Conclusions

This work provides insight into the underlying physics that connects the albedo-area as seen by the observer to the SRP albedo-area. There is a physical connection between SRP albedo-area which drives SRP forces experienced by a given space object, and its observed albedo-area. The net SRP force is caused due to absorption and reflection (diffuse and/or specular) of incident radiation from the surface of an object. If we ignore the contribution of transmissivity, the total energy exchanged due to absorption and reflection can be constrained to unity and this constraint can be exploited. The physical connection between SRP and Observed albedo-area then allows us (in theory) to estimate the space object's mass, only observable by way of the mutual information contained in combined astrometric and photometric data. It is important that the SRP force model use the same BRDF as the observed albedo-area measurement formulation.

The results show that while considering the area of an RSO effects the observability and estimates for mass, we can still get meaningful results for satellite characterization and mass as the uncertainties are lowered from the initial value of 800 kg to lower values. However, not considering

the area causes the filter to diverge, and although the parameter uncertainties for this case are much smaller, there is no confidence associated with the results.

Acknowledgements

This research was conducted through funding provided by Dr. Stacie Williams under AFOSR award no. FA9550-18-1-0351, and the University of Texas at Austin. The authors would like to thank Dr. Stacie Williams, AFOSR, and the University of Texas at Austin for supporting this work. The authors would also like to thank Dr. Tamara Payne for useful discussions on some of the topics addressed in this work.

Appendix A. Histograms of parameter uncertainties and error RMS values

See Figs. A1–A8.

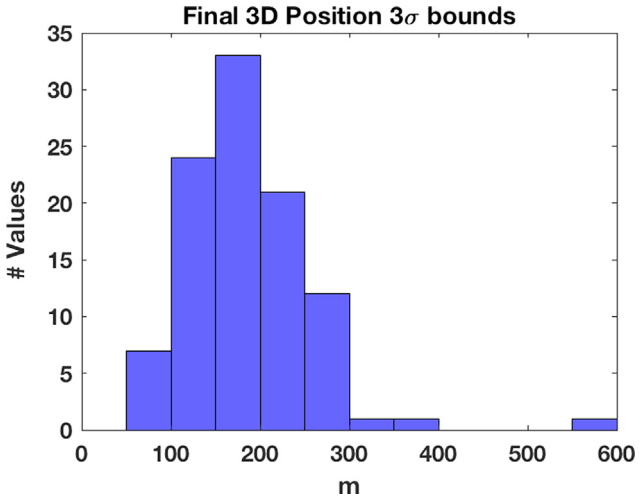

Fig. A1. Histogram of values for final 3σ uncertainty in position (3D).

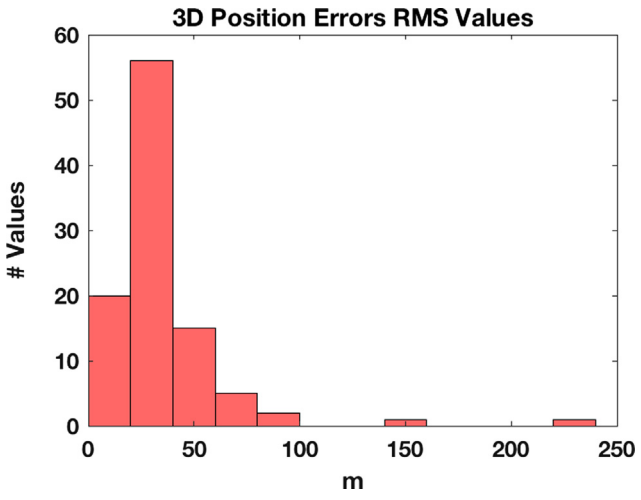

Fig. A2. Histogram of position error RMS values.

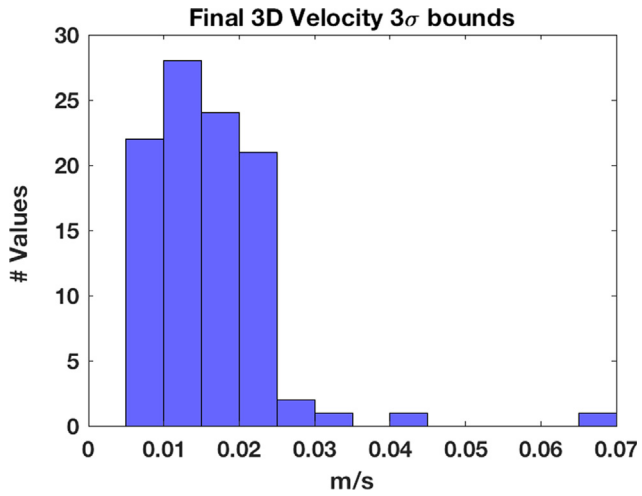

Fig. A3. Histogram of values for final 3σ uncertainty in velocity (3D).

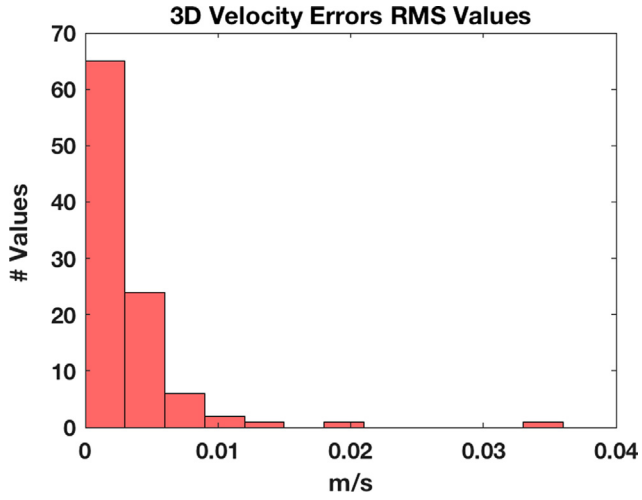

Fig. A4. Histogram of velocity error RMS values.

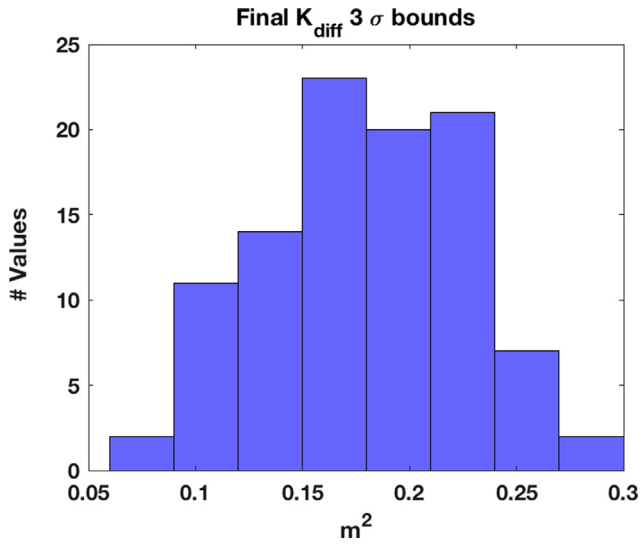

Fig. A5. Histogram of values for final 3σ uncertainty in diffuse albedo-area.

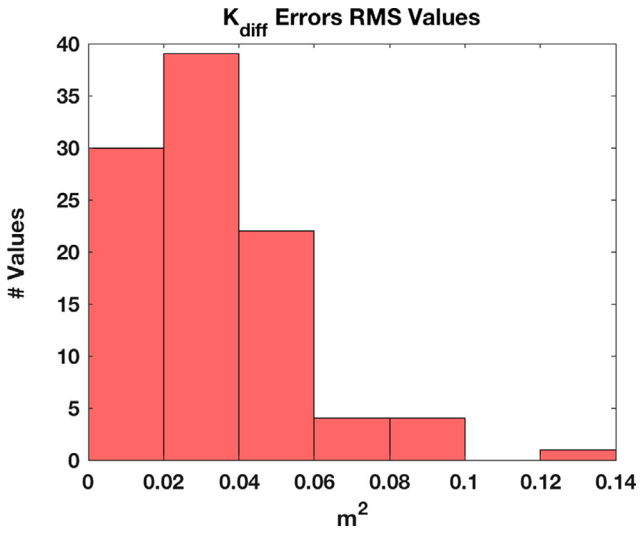

Fig. A6. Histogram of diffuse albedo-area error RMS values.

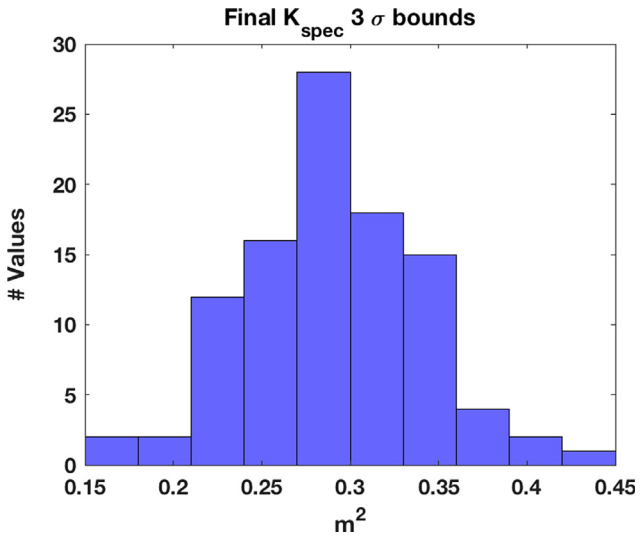

Fig. A7. Histogram of values for final 3σ uncertainty in specular albedo-area.

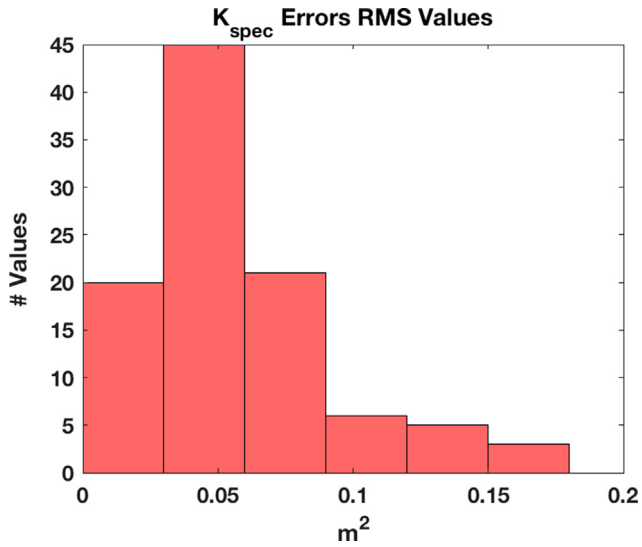

Fig. A8. Histogram of specular albedo-area error RMS values.

References

Jah, M., Madler, R., 2007. Satellite characterization: angles and light curve data fusion for spacecraft state and parameter estimation. In: Proceedings of the Advanced Maui Optical and Space Surveillance Technologies Conference, Wailea, Maui, HI.

Jah, M. Congressional Witness, invited by U.S. Senator Ted Cruz (R-Texas), chairman of the Subcommittee on Space, Science, and Competitiveness, to provide testimony at the Reopening the American Frontier: Promoting Partnerships Between Commercial Space and the U.S. Government to Advance Exploration and Settlement, 13 July 2017.

Joint Chiefs of Staff. Space Operations. Joint Publication 3–14, May 2013. Retrieved from <http://www.dtic.mil/doctrine/new_pubs/jp3_14.pdf>.

Linares, R., Jah, M., Crassidis, J., Leve, F., Kelecy, T., 2014. Astrometric and photometric data fusion for inactive space object mass and area estimation. J. Int. Acad. Astronaut.: Acta Astronaut. 99, 1–15.

Linares, R., Crassidis, J. L., Wetterer, C. J., Hill, K., Jah, M. K., 2013. Astrometric and photometric data fusion for mass and surface material estimation using refined bidirectional reflectance distribution functions-solar radiation pressure model. In: Proceedings of the Advanced Maui Optical and Space Surveillance Technologies Conference, Wailea, Maui, HI.

Lyon, R.H., 2002. Geosynchronous Orbit Determination Using Space Surveillance Network Observations and Improved Radiative Force Modeling Masters thesis. Massachusetts Institute of Technology.

McMahon, J.W., Scheeres, D.J., 2015. Improving space object catalog maintenance through advances in solar radiation pressure modeling. AIAA J. Guid. Control Dynam. 38 (8), 1366–1381.

Kandepu, R., Imsland, L., Foss, B.A., 2008. Constrained state estimation using the unscented Kalman filter. In: Proceedings of the 2008 16th Mediterranean Conference on Control and Automation, Ajaccio.

Schildknecht, T., Musci, R., Ploner, M., Beutler, G., Flury, W., Kuusela, J., de Leon Cruz, J., de Fatima Dominguez Palmero, L., 2004. Optical observations of space debris in GEO and in highly-eccentric orbits. Adv. Space Res. 34 (5), 901–911.

Stauch, J., Jah, M., 2015. Unscented schmidt-Kalman filter algorithm. AIAA J. Guid. Control Dynam. 38 (1), 117–123.

Wetterer, C.J., Jah, M., 2009. Attitude estimation from light curves. AIAA J. Guid. Control Dynam. 32 (5), 1648–1651.

Wetterer, C., Linares, R., Crassidis, J., Kelecy, T., Ziebart, M., Jah, M., Cefola, M., 2013. Refining space object radiation pressure modeling with bidirectional reflectance distribution functions. AIAA J. Guid. Control Dynam. 37 (1), 185–196.

Ziebart, M., 2004. Generalized analytical solar radiation pressure modeling algorithm for spacecraft of complex shape. J. Spacecraft Rock. 41 (5), 840–848.